crystals

MDPI

Article

Tailoring the Microstructure and Mechanical Properties of Laser Directed Energy–Deposited Inconel 718 Alloys via Ultrasonic Frequency Modulation

Bo Peng [1], Mengmeng Zhang [2], Xiaoqiang Zhang [3], Ze Chai [4,*], Fahai Ba [5] and Xiaoqi Chen [1,6,*]

1 Shanghai Key Laboratory of Materials Laser Processing and Modification, School of Materials Science and Engineering, Shanghai Jiao Tong University, 800 Dongchuan Road, Shanghai 200240, China; pengbhit@sjtu.edu.cn
2 Department of Micro/Nano Electronics, School of Electronic Information and Electrical Engineering, Shanghai Jiao Tong University, 800 Dongchuan Road, Shanghai 200240, China; wawjzmm2011@163.com
3 School of Materials Science and Engineering, Jiangsu University of Science and Technology, Zhenjiang 212000, China; 202100000022@just.edu.cn
4 School of Aerospace Engineering and Applied Mechanics, Tongji University, 100 Zhangwu Road, Shanghai 200092, China
5 Shanghai Research Institute of Materials Co., Ltd., 99 Handan Road, Shanghai 200433, China; bafahai@163.com
6 Shien-Ming Wu School of Intelligent Engineering, South China University of Technology, Guangzhou 511442, China
* Correspondence: chaize@tongji.edu.cn (Z.C.); xqc@scut.edu.cn (X.C.)

Abstract

Ultrasonic-assisted laser-directed energy deposition (UA-DED) is a promising combined technology for manufacturing high-value thin-walled Inconel 718 components in aerospace. Nevertheless, the optimal ultrasonic frequency—a key parameter for achieving desirable performance in thin-walled Inconel 718 alloys—remains to be determined. In this study, we systematically investigated the influence of ultrasonic frequency (12–20 kHz) on the microstructure and mechanical properties of thin-walled Inconel 718 fabricated by UA-DED. The results revealed that an ultrasonic frequency of 20 kHz was optimal and can yield significant improvements in the microstructures of the as-deposited sample coordinate planes, manifested by the complete suppression of large pores, three-dimensional refinement of the γ matrix grains, alleviation of Nb and Mo segregation, the reduction of fragmented Laves particles, a decrease in residual macroscopic stresses, and homogeneous distributions of γ'/γ'' phases and γ-grain orientation. Meanwhile, the application of a 20 kHz ultrasonic frequency endows the manufactured thin-walled 718 parts with superior mechanical properties, including a tensile strength of 899 MPa in the laser scanning direction and 877 MPa in the build direction, along with the corresponding elongations of 34.8% and 38.9%. This work demonstrates the potential of modulating ultrasonic frequency to tailor microstructures and produce high-performance thin-walled Inconel 718 aerospace components.

Keywords: laser-directed energy deposition; Inconel 718; thin-walled component; ultrasonic frequency; microstructure; mechanical property

Check for updates

Academic Editor: Marek Sroka

Received: 4 January 2026
Revised: 18 January 2026
Accepted: 19 January 2026
Published: 21 January 2026

Copyright: © 2026 by the authors. Licensee MDPI, Basel, Switzerland. This article is an open access article distributed under the terms and conditions of the Creative Commons Attribution (CC BY) license.

1. Introduction

Inconel 718, a nickel-based superalloy strengthened by γ' (Ni_3 (Al, Ti)) and γ'' (Ni_3Nb) precipitates, exhibits a high specific strength along with outstanding oxidation and corrosion resistance [1]. These properties make it an ideal material for critical aerospace

components such as combustor casings, seals, and disk- or ring-type parts, especially in the thin-walled configurations [2–4]. The fabrication of such high-value thin-walled Inconel 718 components increasingly relies on advanced intelligent manufacturing technologies, among which laser-directed energy deposition (DED) has seen particularly rapid development in recent years [5]. In the DED process, Inconel 718 powders are continuously fed into the interaction zone of a focused laser beam, forming a localized molten pool on the substrate. As the laser follows a pre-programmed path, the melt pool rapidly solidifies and overlaps with adjacent tracks. Through successive layer-by-layer deposition, near-net-shape Inconel 718 components can be efficiently fabricated [6–8]. Consequently, DED technology is particularly well-suited for producing complex-shaped, thin-walled Inconel 718 parts.

However, several critical challenges remain to be addressed in the DED of Inconel 718. The rapid solidification inherent to the DED process typically produces microstructures dominated by coarse columnar dendrites and a strong crystallographic texture [9,10]. Most importantly, during service, thin-walled Inconel 718 components are often subjected to combined thermal gradients, dwell periods, and cyclic mechanical loads [11,12]. Compared to the bulk sections, these thin-walled geometries exhibit heightened sensitivity to the microstructural features and defects introduced during manufacturing [13]. Specifically, the non-equilibrium solidification promotes microsegregation of alloying elements such as Nb and Mo in interdendritic regions [14]. This segregation facilitates the formation and coarsening of the brittle Laves phase (Ni, Fe, Cr)$_2$(Nb, Mo, Ti) [15]. The Laves phase is a type of hard and brittle intermetallic compound that can markedly deteriorate the mechanical performance of as-deposited Inconel 718 [16]. Moreover, the intense local heating followed by rapid cooling under a high thermal gradient generates high residual tensile stresses in the as-deposited parts [17]. Furthermore, defects, particularly the pervasively formed pores during deposition, critically undermine the in-service reliability of Inconel 718 components [18].

To address these challenges, the introduction of ultrasonic vibration during DED, namely ultrasonic-assisted DED (UA-DED), has emerged as an effective in situ control strategy [19–21]. This approach primarily relies on two ultrasonic effects, cavitation and acoustic streaming [22]. When the ultrasonic intensity surpasses the cavitation threshold of the melt pool, the alternating acoustic pressure promotes the formation, oscillation, and eventual collapse of bubbles, thereby enhancing nucleation and fragmenting semi-solid dendrite arms [23,24]. Meanwhile, the acoustic streaming induces strong, steady convection within the melt pool. This significantly enhances the heat and mass transfer and weakens the thermal boundary layer and thus suppresses the excessively epitaxial growth while refining the grains [25,26]. Several researchers have carried out key preliminary investigations into UA-DED. Ning et al. [27] found that the ultrasonic vibration during Inconel 718 DED facilitated the dissolution of detrimental coarse Laves phases. This retains more Nb in the γ matrix for subsequent γ' precipitation, ultimately enhancing the yield strength (YS) and ultimate tensile strength (UTS) after heat treatments. Moreover, UA-DED has proven effective in suppressing process-induced microstructure defects [28,29]. Our previous study [30] demonstrated that the ultrasonic vibration substantially reduces the porosity of additively manufactured Inconel 718 alloys.

Nevertheless, the existing research is largely limited to the simple comparison of Inconel 718 DEDed with and without ultrasonic vibration [27–32] or focuses on bulk Inconel 718 DEDed with remarkably high ultrasonic frequencies above 25 kHz [33,34]. As a key process parameter, optimal ultrasonic frequency and its effects on the microstructure and property of the thin-walled Inconel 718 have not yet been elucidated. Here, we systematically characterize the microstructure and mechanical properties of UA-DED thin-

walled Inconel 718 samples under ultrasonic frequency modulation. The optimal frequency is identified and used to achieve superior microstructures and mechanical properties. This work demonstrates that modulating ultrasonic frequency enables precise control over microstructure evolution, providing a viable pathway toward the manufacture of high-performance thin-walled Inconel 718 components for aerospace applications.

2. Methods

2.1. Materials

The Inconel 718 powder used in this study was commercially produced via gas atomization (AVIC Mate Powder Metallurgy Technology Co., Ltd., Beijing, China). The elemental composition of the powder is provided in Table 1. The powder had a spherical morphology and a size distribution of 53–150 μm. Prior to deposition, it was vacuum-dried at 150 ± 10 °C for 2 h. The substrate material was 316L stainless steel. It was mechanically ground and then cleaned with acetone to remove surface oxides and contaminants.

Table 1. Elemental composition of Inconel 718 powders (wt.%).

Elements	Cr	Nb	Mo	Al	Ti	Mn	Si	C	Fe	Ni
Inconel 718 powder	19.79	5.13	2.95	0.52	1.07	0.01	0.04	0.03	17.45	Bal.

2.2. UA-DED Setup and Procedure

The overall DED setup is illustrated in Figure 1. The DED system was assembled from commercial modules (Nanjing Zhongke Raycham Laser Technology Co., Ltd., Nanjing, China). A 2000 W fiber laser (IPG YLS-2000-CT, wavelength 1070 nm) served as the heat source. The motion was controlled by a 6-axis robotic arm (KUKA KR30HA), which manipulated a coaxial deposition nozzle (PRECITEC YC52). The powders were delivered by a triple-hopper feeder (RC-PGF-D) using high-purity argon (99.99%) as both the carrier and shielding gas.

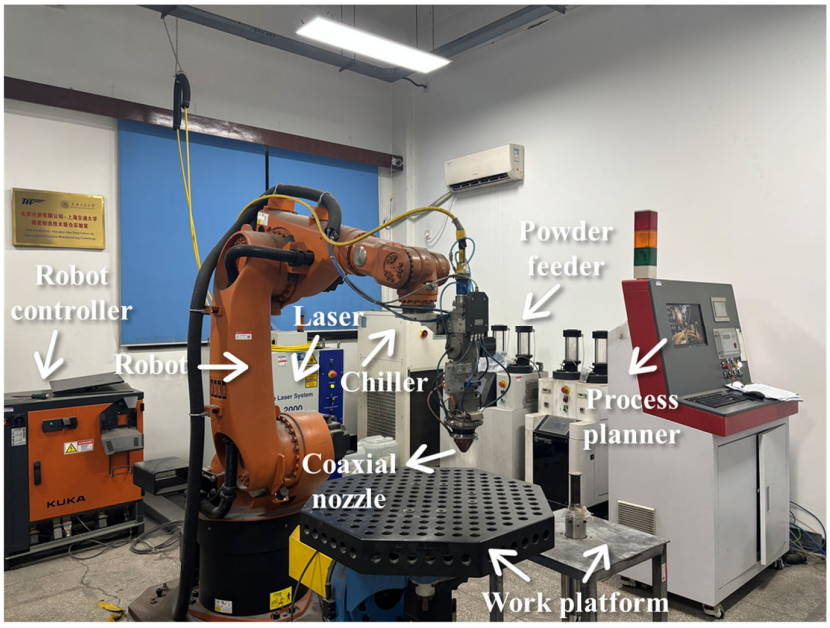


Figure 1. Overview of the DED setup.

The ultrasonic system consisted of a power supply (Figure 2a) and an integrated transducer assembly mounted on a vibration table (Figure 2b), with a rated power of

4.8 kW and an operating voltage of 220 V. To ensure efficient vibration transmission into the melt pool, the ultrasonic horn was secured via a coupling sleeve and brought into rigid contact with the substrate. The ultrasonic frequency was set to 12 kHz, 16 kHz, or 20 kHz. It should be noted that 20 kHz is the upper limit of the ultrasonic frequency, as stable fabrication of thin-walled parts became challenging beyond this value. Based on the ultrasonic frequencies used, the as-deposited samples were named as 12-UA-DED, 16-UA-DED, and 20-UA-DED. A bidirectional scanning strategy was applied, and other key deposition parameters were as follows: a laser power of 320 W, a scan speed of 4 mm·s^{-1}, a spot diameter of 1.6 mm, a hatch spacing of 1 mm, a powder feed rate of 7.2 g·min^{-1}, and a layer height of 0.42 mm.

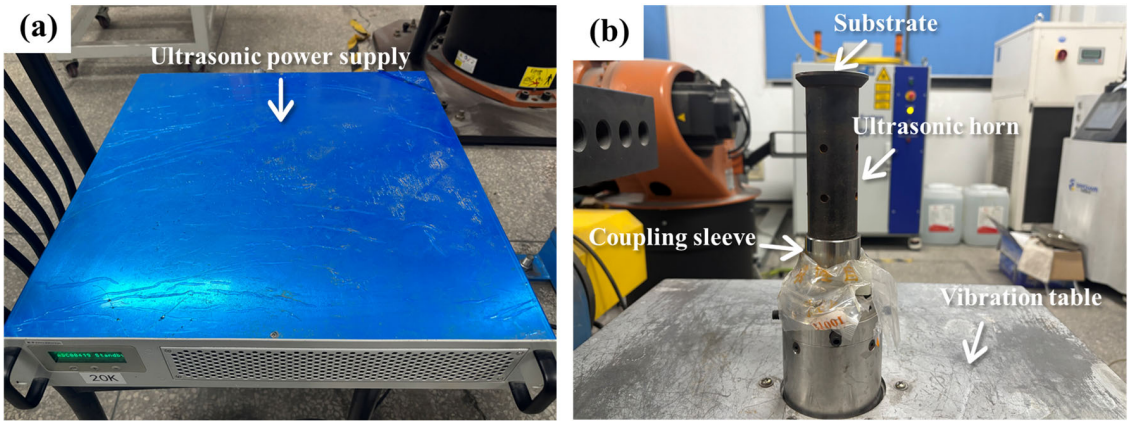


Figure 2. Ultrasonic system used in this study: (**a**) ultrasonic power supply and (**b**) ultrasonic integrated setup, consisting of the substrate, ultrasonic horn, coupling sleeve, and vibration table.

2.3. Microstructure Characterization

In this study, thin-walled Inconel 718 geometry (Figure 3a) with dimensions of 40 mm length (along the laser scan direction, i.e., X direction in Figure 3b) × 25 mm height (along the build direction, i.e., Z direction in Figure 3b) × 2 mm thickness (along the transverse direction, i.e., Y direction in Figure 3b) was fabricated. The Inconel 718 samples for microstructural analysis were cut from the middle region of the thin-walled geometry. The middle region was selected to eliminate the boundary effects from the start and termination of deposition. The microstructures of three sample coordinate planes (i.e., Z–X, Z–Y, and X–Y planes in Figure 3b) of the samples were examined. Following conventional mechanical grinding and polishing, the samples were electrolytically etched in a 10% oxalic acid solution (Shanghai Aladdin Biochemical Technology Co., Ltd., Shanghai, China) at 4 V for 15 s. Microstructural examination was conducted using an optical microscope (OM, Carl Zeiss AxioCam-MRc5, Carl Zeiss AG, Jena, Germany) and a scanning electron microscope (SEM, TESCAN MIRA3, TESCAN, Brno, Czech Republic). The SEM was equipped with both an energy-dispersive spectrometer (EDS, Aztec X-MaxN8, Oxford Instruments, Abingdon, UK) and an electron backscatter diffraction detector (EBSD, Oxford Instruments Aztec Nordys-max3, Oxford Instruments, Abingdon, UK). For crystallographic texture and local strain analysis, EBSD mapping was performed with a step size of 1.75 μm under an accelerating voltage of 20 kV. Prior to EBSD analysis, the samples were electropolished using an electrolyte composed of 10% $HClO_{4-}$ (Shanghai Aladdin Biochemical Technology Co., Ltd., Shanghai, China) and 90% CH_3OH (Shanghai Aladdin Biochemical Technology Co., Ltd., Shanghai, China) (by volume) at 10 V for 120 s. The phase identification was performed using X-ray diffraction (XRD, Rigaku Ultima IV, Rigaku Corporation, Tokyo, Japan) with Cu K_α radiation (λ = 1.54056 Å) and a step size of 0.02° at 40 kV and 30 mA.

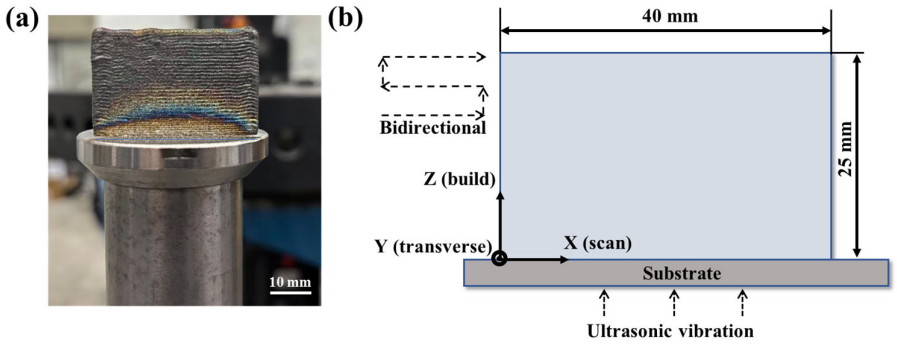


Figure 3. (**a**) Macroscopic image and (**b**) schematic diagram of the deposited thin-walled Inconel 718 samples.

Besides the aforementioned microstructures, the residual macroscopic stress was measured at the Z–X plane center using an X-ray diffractometer (Proto Manufacturing Ltd., Tecumseh, ON, Canada) using the $\sin^2\psi$ method. The stress measurements were conducted on the (311) plane of the face-centered cubic Ni using Mn K_α radiation (λ = 2.10314 Å). Prior to the stress test, the sample surfaces were electropolished to eliminate the unmelted alloy particles.

2.4. Mechanical Property Assessment

Tensile tests were conducted at room temperature using an INSTRON 5966 universal testing machine (Instron, Boston, MA, USA) under a constant loading rate of 0.6 mm/min. Tensile strain was recorded using a non-contact video extensometer (Instron Advanced Video Extensometer AVE 2, Boston, MA, USA) with a displacement resolution of 1 μm. Tensile testing was conducted along two orthogonal orientations: the X and Z directions (Figure 3b). The dimensions of the tensile sample are depicted in Figure 4. The sample was extracted from the middle region of the thin-walled geometries, with the center of its gauge section located 12.5 mm from the substrate. Tensile tests along the X or Z direction were repeated three times to ensure high reproducibility and reliability of the reported results. The fracture morphology was examined using SEM.

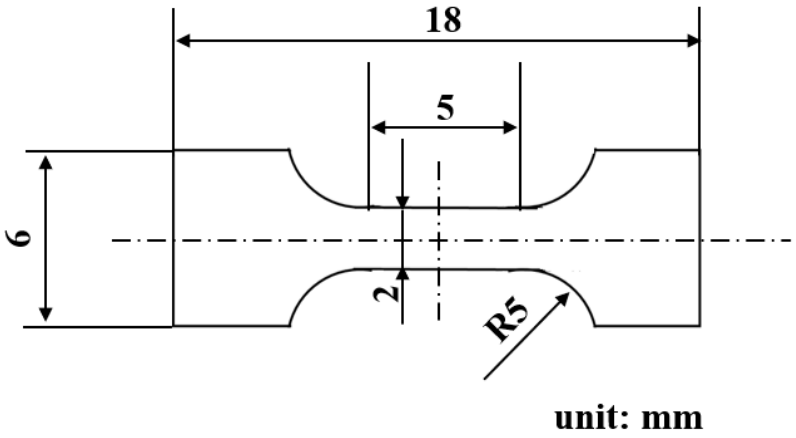


Figure 4. The sample dimension for tensile tests.

3. Results

3.1. OM Analysis

Figure 5 presents the pore characteristics of the thin-walled Inconel 718 samples deposited under ultrasonic frequency modulation. Obviously, large pores of approximately 100 μm were observed across the Z–X, X–Y, and Z–Y planes of the 12-UA-DED sample

(Figure 5a–c), and they were also visible on the Z–X and X–Y planes of the 16-UA-DED sample (Figure 5d,e). In particular, these large pores were absent on all coordinate planes of the 20-UA-DED sample, where only small spherical pores were observed (Figure 5g–i).

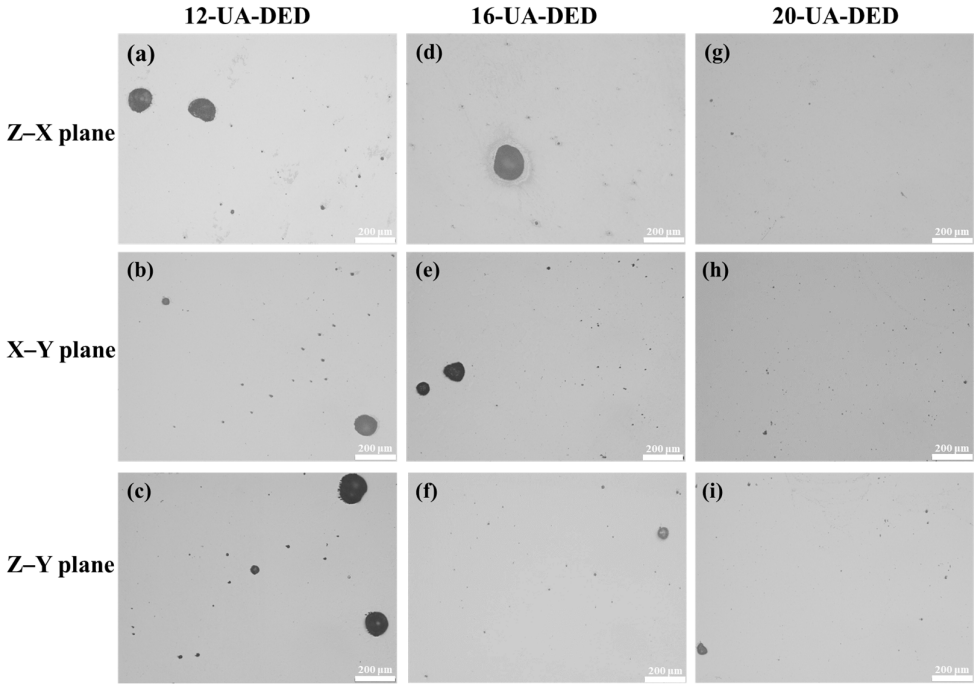


Figure 5. Pore analysis of the thin-walled Inconel 718 samples: (**a**–**c**) 12-UA-DED, (**d**–**f**) 16-UA-DED, and (**g**–**i**) 20-UA-DED.

The probability density function of pore size in the UA-DED thin-walled Inconel 718 samples is shown in Figure 6a, with no differentiation between the Z–X, X–Y, and Z–Y planes due to negligible differences in the pore data. It can be seen that the pore sizes of all samples were predominantly smaller than 12 μm. As the ultrasonic frequency increased, the pore size distribution shifted toward a small-sized zone, with the size of less than 2 μm being predominant in the 20-UA-DED sample. The relevant porosity analysis results are summarized in Figure 6b. The porosity decreased monotonically with increasing the frequency, i.e., declining from 0.86% at 12 kHz to 0.72% at 16 kHz and 0.08% at 20 kHz. Note that the porosity decrease was minor from 12 kHz to 16 kHz, while at 20 kHz, the porosity dropped by roughly one order of magnitude compared to those at the two low frequencies. This finding demonstrated the remarkable densification effect from the ultrasonic frequency approaching 20 kHz.

The pore analysis results indicated that the application of the 20 kHz frequency markedly and effectively suppresses the large-pore formation in the thin-walled Inconel 718 samples. It seems that at 16 kHz and below, the acoustic streaming is weak and unable to efficiently propel the entrapped bubbles. Consequently, these bubbles may be retained near the alloy solidification front (e.g., in interdendritic regions and along the melt-pool boundary), where they could coalesce into large-sized ones [35]. When the applied frequency is increased to 20 kHz, the ultrasonic input is expected to exceed the melt-pool cavitation threshold, thereby maximizing the cavitation effect [36]. The subsequent oscillation and collapse of cavitation bubbles can produce pressure pulses and micro-jets, which effectively fragment and disperse the entrapped bubbles [37]. On the other hand, the intense acoustic streaming can enhance the melt-pool convection and solute transport [38], further suppressing bubble retention and growth before terminal

alloy solidification. Therefore, the pores are basically smaller and fewer in the 20-UA-DED thin-walled Inconel 718 alloys.

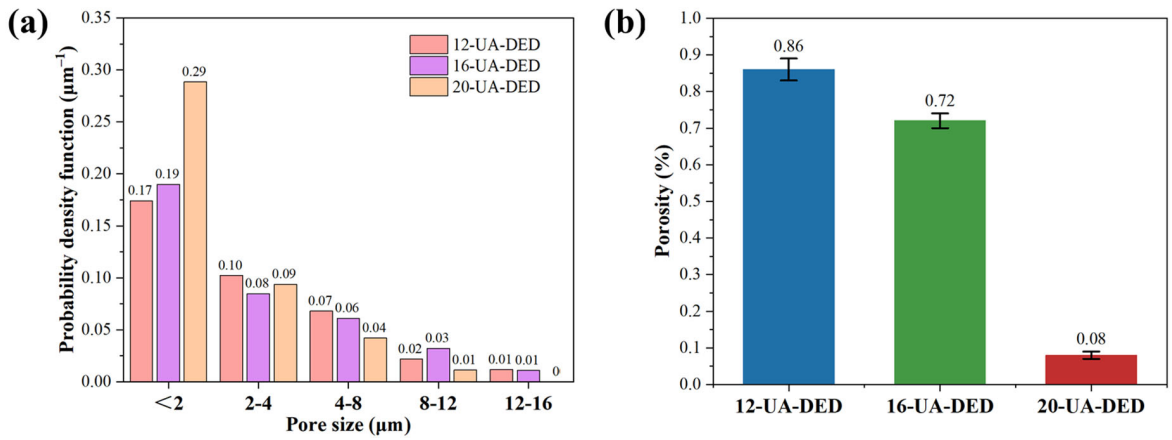


Figure 6. (**a**) Probability density function of the pore size and (**b**) porosity of the UA-DED thin-walled Inconel 718 samples.

3.2. XRD Analysis

Figure 7 displays the XRD patterns of the thin-walled Inconel 718 samples deposited via ultrasonic frequency modulation. The primary diffraction peaks corresponding to the face-centered cubic γ matrix—(111), (200), and (220)—were clearly seen on the Z–X, X–Y, and Z–Y planes of the three samples, and the Laves phase is also identified. It is difficult to differentiate the matrix γ and the precipitates γ′ and γ″ due to their similar lattice parameters [39]. Moreover, the δ phase or MX carbides or nitrides cannot be identified, probably due to their low volume fractions of less than 3%.

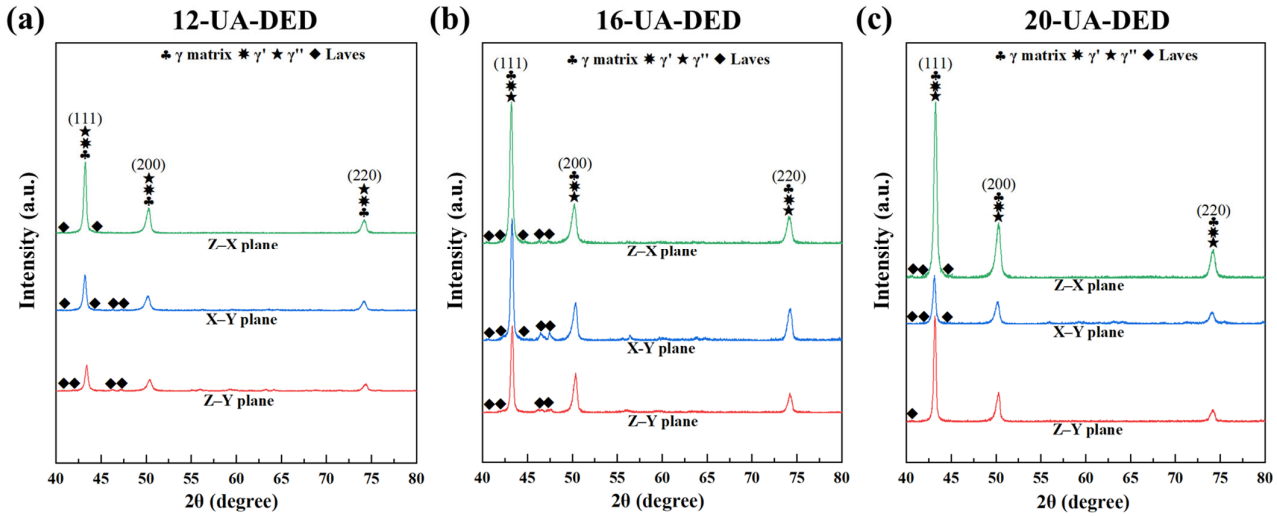


Figure 7. XRD patterns of the thin-walled Inconel 718 samples: (**a**) 12-UA-DED, (**b**) 16-UA-DED, and (**c**) 20-UA-DED.

The crystal perfection of a metal or alloy can be reflected by the broadening of its diffraction peak profiles, typically represented by the full width at half maximum (FWHM) of the profiles [40]. The peak profile broadening is primarily attributed to the combined effects of the domain size and microstrain [41]. Here, we determined the FWHM of the (111) diffraction peaks for all UA-DED thin-walled Inconel 718 samples using a pseudo-Voigt function, after deducting the background and $K_{\alpha 2}$ component from the measured peak. As

seen from Table 2, on the Z–X plane, the FWHM monotonically increased from 0.317° to 0.393° when increasing the ultrasonic frequency from 12 kHz to 20 kHz, on the Z–Y plane it decreased from 0.372° to 0.304° with the ultrasonic frequency, and on the X–Y plane it exhibited a nonlinear variation with frequency.

Table 2. FWHMs of the (111) diffraction peaks for UA-DED thin-walled Inconel 718 samples.

Samples	Plane	FWHM of (111) Diffraction Peak (°)
12-UA-DED	Z–X	0.317 (±0.004)
12-UA-DED	X–Y	0.377 (±0.004)
12-UA-DED	Z–Y	0.372 (±0.004)
16-UA-DED	Z–X	0.359 (±0.005)
16-UA-DED	X–Y	0.313 (±0.004)
16-UA-DED	Z–Y	0.308 (±0.004)
20-UA-DED	Z–X	0.393 (±0.005)
20-UA-DED	X–Y	0.374 (±0.004)
20-UA-DED	Z–Y	0.304 (±0.003)

The FWHM variations in the (111) diffraction peaks for UA-DED Inconel 718 samples indicated coordinate plane- and ultrasonic frequency-dependent microstructural evolution during manufacturing. Specifically, the Z–X plane corresponds to the cross-section of melt pools, and it is thought to experience intense agitation from ultrasonic vibration under a high frequency of 20 kHz. This intense agitation could reduce the domain size and increase the microstrain [42], thus deteriorating the crystal perfection to some extent and leading to severe peak profile broadening. For the Z–Y plane, the heat dissipation along the thickness direction is extremely constrained during deposition. A high ultrasonic frequency may produce great energy into the melt pool, which may cause subsequent microstructure recovery [43] on the heat dissipation-limited plane. Consequently, the high frequency of 20 kHz can improve the crystal perfection on the Z–Y plane; the relevant sample had a small FWHM value. Additionally, on the X–Y plane, the (111) peak broadening might not be governed simply by the intense melt pool agitation (on the Z–X plane) or by the thermal-assisted microstructure recovery (on the Z–Y plane); it exhibited a nonlinear relation with the ultrasonic frequency.

On the other hand, for all UA-DED thin-walled Inconel 718 samples, the intensity ratio of the (111) to (200) diffraction peaks ranged from 2.20 to 3.74, which was close to 2.38 of the standard reference Ni, indicating negligible crystallographic texture in these samples.

3.3. SEM Analysis

Figure 8 shows the SEM morphologies of Laves phases in the thin-walled Inconel 718 samples deposited under ultrasonic frequency modulation. It can be seen that the ultrasonic vibration fragmented the Laves phase into discrete particles with a short chain, contrasting with the continuous, long-chain Laves phase typically found in conventional DED alloys [30]. As the ultrasonic frequency increased from 12 kHz to 20 kHz, the fraction of the Laves phase decreased, and further refinement of this phase was evident when the frequency was modulated from 16 kHz to 20 kHz. These frequency-dependent changes in the Laves phase morphology were associated with the extent of elemental segregation during deposition [14]; particularly, the high frequency of 20 kHz might effectively alleviate the local Nb/Mo enrichments required for Laves-phase nucleation and growth.

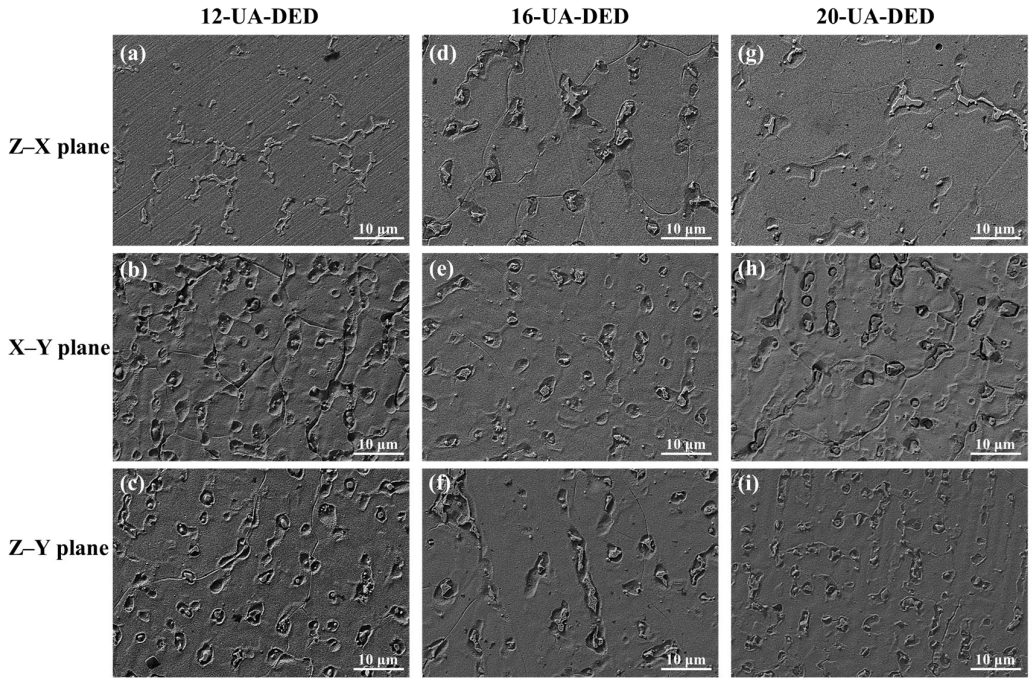


Figure 8. SEM morphologies of Laves phases in thin-walled Inconel 718 samples: (**a**–**c**) 12-UA-DED, (**d**–**f**) 16-UA-DED, and (**g**–**i**) 20-UA-DED.

Figure 9 depicts the morphologies of the γ'/γ'' precipitates around the Laves phase in the UA-DED thin-walled Inconel 718 samples. In the 12-UA-DED sample (Figure 9a), the γ'/γ'' precipitates exhibited inhomogeneous sizes, and for the 20-UA-DED sample in Figure 9b, these precipitates, with an average size of approximately 10 nm, distributed uniformly. This finding demonstrated that high-frequency ultrasonic-assisted deposition improves the homogeneity of γ'/γ'' precipitation. Intuitively, the high-frequency ultrasonic vibration could provide great energy input during deposition, which effectively lowers the nucleation barriers [44,45] of γ'/γ'' precipitates. On the other hand, at 20 kHz, the intense melt-pool convection could enhance the solute redistribution near the Laves phase and increase the density of nucleation sites, thus resulting in a uniform size distribution of γ'/γ'' precipitates.

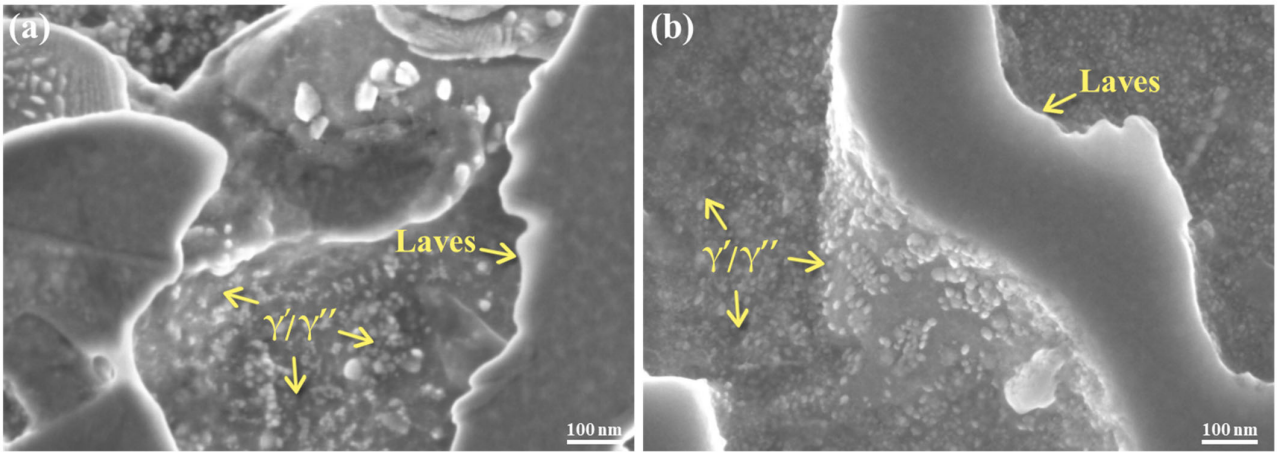


Figure 9. SEM morphologies of γ'/γ'' precipitates in thin-walled Inconel 718 samples: (**a**) 12-UA-DED and (**b**) 20-UA-DED.

3.4. EDS Analysis

Figure 10 displays the EDS analysis of the thin-walled Inconel 718 samples deposited under ultrasonic frequency modulation. The elemental composition analysis was performed at specific points on the Z–X plane for each sample: points A (γ matrix) and B (Laves phase) for the 12-UA-DED sample, points C (γ matrix) and D (Laves phase) for the 16-UA-DED sample, and points E (γ matrix) and F (Laves phase) for the 20-UA-DED sample. The results of EDS analysis are summarized in Table 3. Additionally, the elements Mn, Si, and C were not analyzed, considering their extremely low contents. The EDS analysis results indicated that, relative to the γ matrix, the Laves phase was strongly enriched in Nb, Mo, and Ti but depleted in Cr, Fe, and Al. This finding aligns well with the typical elemental composition of Laves phase precipitates from the matrix alloy. Moreover, with increasing the ultrasonic frequency, the Nb content in the γ matrix increased from 2.3 wt.% at 12 kHz to 4.0 wt.% at 16 kHz and further to 4.7 wt.% at 20 kHz, while in the Laves phase it decreased from 28.3 wt.% to 26.5 wt.% and then to 21.2 wt.%, accordingly. This demonstrated the significant alleviation of Nb aggregation in the high-frequency UA-DED sample. Furthermore, compared with Nb, Mo exhibited slight mitigation in segregation, possibly due to its lower diffusivity and high atomic mass [46].

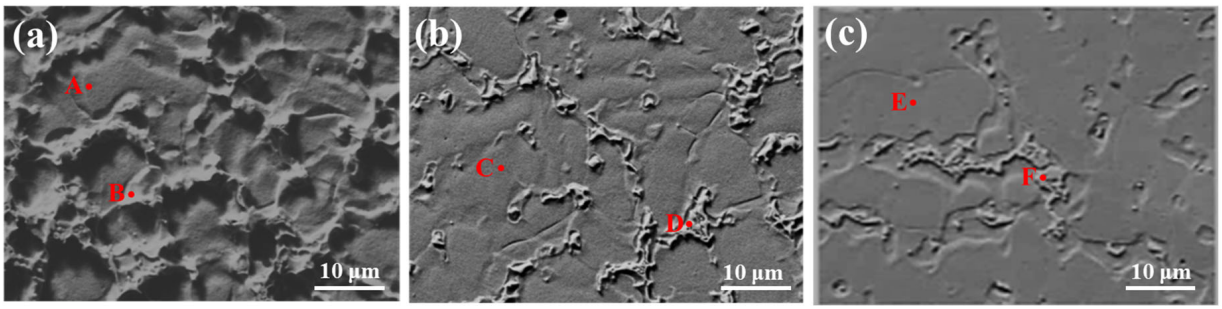


Figure 10. EDS analysis of the thin-walled Inconel 718 samples: (**a**) point A corresponding to γ matrix and point B to Laves phase in 12-UA-DED sample, (**b**) point C corresponding to γ matrix and point D to Laves phase in 16-UA-DED sample, and (**c**) point E corresponding to γ matrix and point F to Laves phase in 20-UA-DED sample.

Table 3. EDS analysis results of the γ matrix and the Laves phase in the UA-DED thin-walled Inconel 718 samples (wt.%).

Position	Al	Ti	Cr	Fe	Nb	Mo	Ni
A (γ matrix)	0.7	0.6	20.5	20.4	2.3	2.9	Bal.
B (Laves)	0.3	1.3	13.8	12.3	28.3	5.4	Bal.
C (γ matrix)	0.8	0.9	19.9	19.1	4	3	Bal.
D (Laves)	0.4	1.4	14.1	12.6	26.5	5.9	Bal.
E (γ matrix)	0.8	1.2	19.9	19	4.7	3.1	Bal.
F (Laves)	0.5	1.4	14.9	13.6	21.2	4.5	Bal.

It is reasonable that at the high ultrasonic frequency of 20 kHz, the intense melt-pool convection effectively promotes the solute transport and mitigates the Nb accumulation in the interdendritic regions during the final stage of solidification [47]. Note that the reduced amount of Nb-rich interdendritic liquid can suppress the formation of continuous, long-chain Laves phases [48]. This was consistent with the discrete, short-chain, and even spherical Laves morphology presented in Figure 8g–i.

3.5. EBSD Analysis

Figure 11 presents the EBSD analysis results of the γ matrix grains in the thin-walled Inconel 718 samples deposited via ultrasonic frequency modulation. As shown in Figure 11a–c, when a 12 kHz ultrasonic frequency was applied, the γ matrix grains remained mostly coarse. Notably, on the Z–Y plane, the coarse columnar grains were largely aligned with the build direction (Figure 11c). However, even at the low frequency of 12 kHz, the ultrasonic assistance promoted a columnar-to-equiaxed transition of γ matrix grains on the Z–X and X–Y planes—a significant difference compared with Inconel 718 deposited without ultrasonic vibration, as specified in our previous work [30]. Moreover, the application of 16 kHz frequency refined the γ matrix grains to a certain extent (Figure 11d–f), and the columnar morphology on the Z–Y plane became less pronounced relative to the 12 kHz frequency case. Furthermore, the 20 kHz frequency ultrasonic-assisted deposition could produce fine, nearly equiaxial γ grains across all coordinate planes, as depicted in Figure 11g–i.

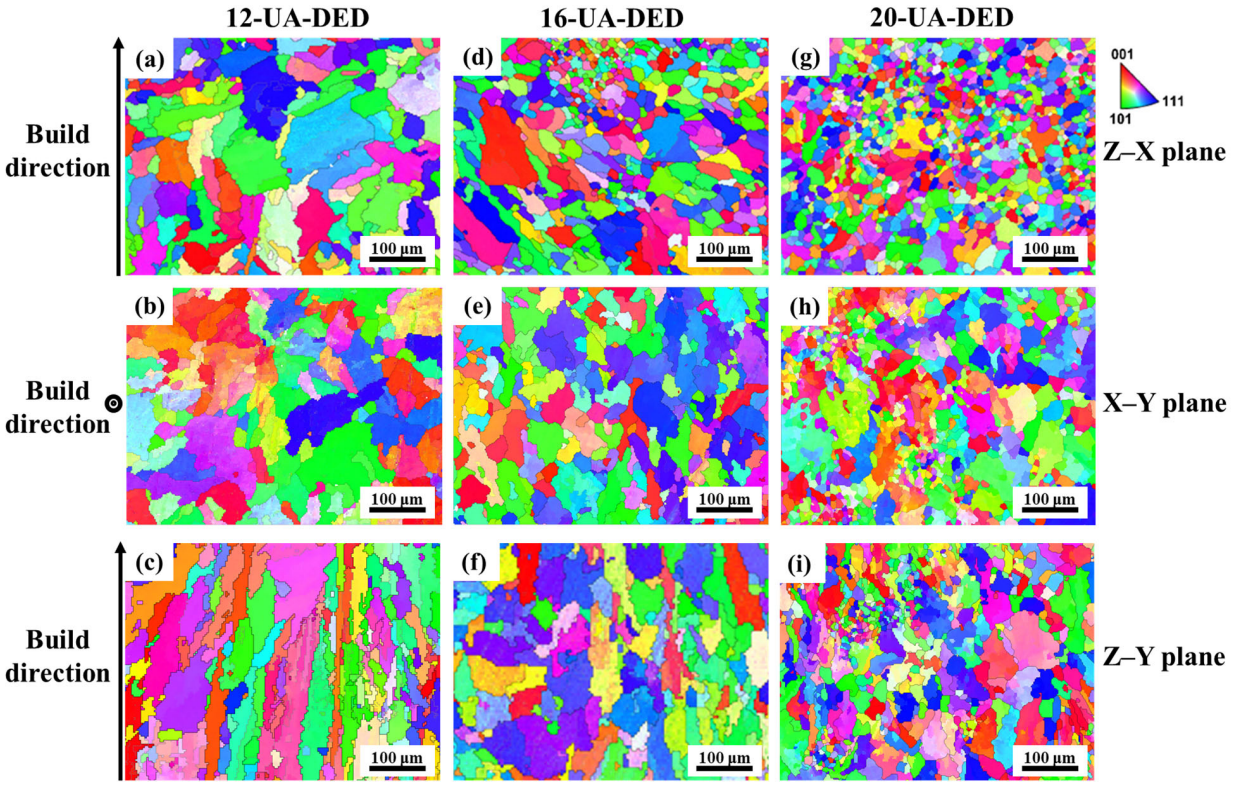


Figure 11. EBSD morphologies of the γ matrix grains in the thin-walled Inconel 718 samples: (**a**–**c**) 12-UA-DED, (**d**–**f**) 16-UA-DED, and (**g**–**i**) 20-UA-DED.

To quantitatively evaluate the geometrical characteristics of the γ matrix grains shown in Figure 11, the mean fitted ellipse major diameter (MD) and mean fitted ellipse aspect ratio (AR) of these grains were determined for the UA-DED thin-walled Inconel 718 samples. As shown in Figure 12a, the 12-UA-DED sample exhibited markedly different MD values across the three coordinate planes, indicating a clear deviation from the desired equiaxed grain morphology. This has not been improved, although the use of a relatively high frequency (16 kHz) could decrease the MD value, except that for the Z–Y plane. It is worth noting that for the 20-UA-DED sample, the MD of γ grains on the Z–Y plane significantly decreased, and by considering the variations for the other two coordinate planes, the application of a high frequency of 20 kHz indeed greatly optimized the three-dimensional morphology of the γ matrix grains. This finding was also verified by the analysis result of AR presented in

Figure 12b. Specifically, when the frequency was modulated from 12 kHz to 16 kHz, the AR values of γ grains remained nearly unchanged on the three coordinate planes, with the Z–Y plane still exhibiting a high AR of approximately 2.7. In contrast, a further increase to 20 kHz led to a clear reduction in AR across all coordinate planes, especially a dramatic decrease of 0.7 for the Z–Y plane. Consequently, the 20-UA-DED sample exhibited low AR values and relatively consistent γ-grain geometries in three dimensions.

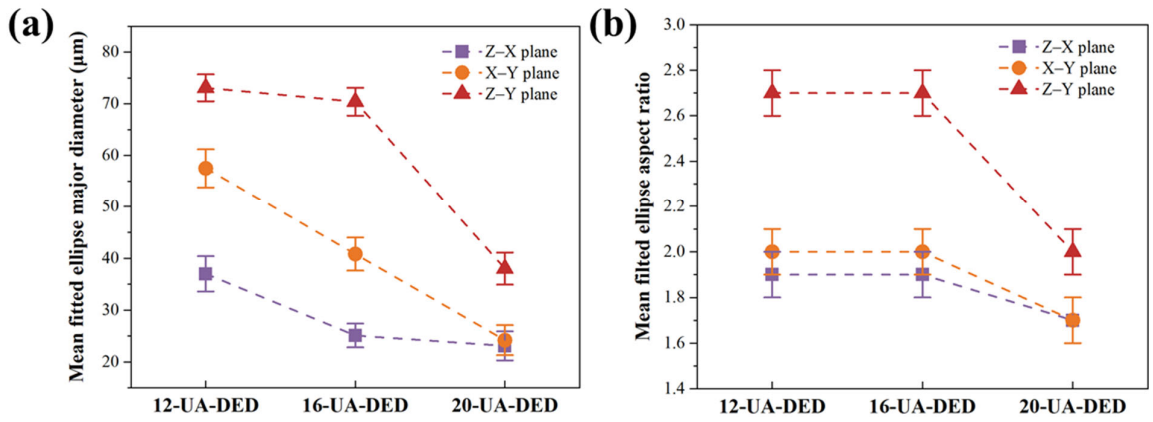


Figure 12. Mean fitted ellipse parameters of γ matrix grains in thin-walled Inconel 718 samples: (**a**) major diameter and (**b**) aspect ratio.

Figure 13 depicts the pole figures of the γ matrix grains in thin-walled Inconel 718 samples deposited under ultrasonic frequency modulation. For these UA-DED samples, the γ matrix grains exhibited a weak crystallographic preferred orientation across each coordinate plane. This finding is consistent with the XRD analysis presented in Section 3.2. Moreover, a striking discrepancy in maximum pole density (MPD) values was observed across the three coordinate planes for the 12-UA-DED sample (e.g., 3.3 on the Z–X plane in Figure 13a versus 6.2 on the X–Y plane in Figure 13b), while the 16- and 20-UA-DED samples exhibited comparable MPD values on all coordinate planes (Figure 13d–i). In addition, the MPD of the γ matrix grains somewhat decreased as the ultrasonic frequency was modulated from 12 kHz to 16 kHz and then to 20 kHz.

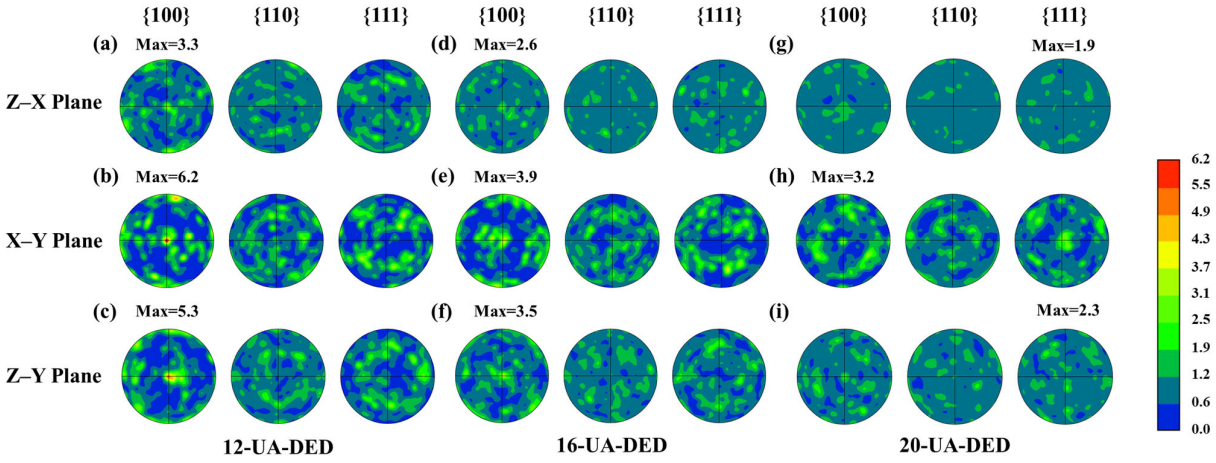


Figure 13. Pole figures of the thin-walled Inconel 718 samples: (**a**–**c**) 12-UA-DED, (**d**–**f**) 16-UA-DED, and (**g**–**i**) 20-UA-DED.

Figure 14 shows the kernel average misorientation (KAM) distributions of the γ matrix grains in thin-walled Inconel 718 samples deposited under ultrasonic frequency modulation. At the low frequencies of 12 kHz and 16 kHz, the KAM of γ grains was distributed

inhomogeneously across the Z–X, X–Y, and Z–Y planes, and it varied significantly for different coordinate planes (Figure 14a–f). Note that the application of 20 kHz markedly homogenized the KAM distribution on each coordinate plane as well as between the coordinate planes (Figure 14g–i). The KAM is generally considered to arise from the presence of geometrically necessary dislocations (GNDs) in crystal structures [49], and its homogeneous distribution in Figure 14g–i implies a uniform three-dimensional arrangement of GNDs in the 20-UA-DED sample. Nevertheless, the KAM values averaged over the three coordinate planes for these UA-DED samples were very close (around 0.5°), indicating a consistent density of GNDs induced by the ultrasonic vibration without frequency dependence.

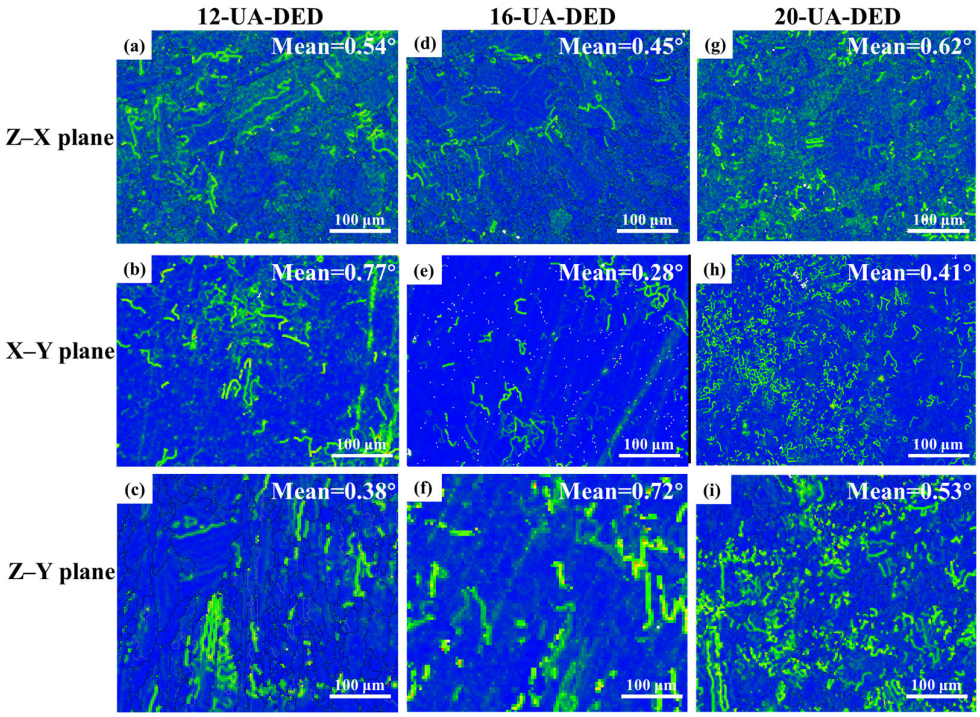


Figure 14. Kernel average misorientation distributions of γ matrix grains in thin-walled Inconel 718 samples: (**a**–**c**) 12-UA-DED, (**d**–**f**) 16-UA-DED, and (**g**–**i**) 20-UA-DED.

The EBSD analysis results demonstrated that applying a high ultrasonic frequency of 20 kHz remarkably refined the γ matrix grains, modified the columnar grain morphology, suppressed the preferential grain growth, and homogenized the GND distribution in three dimensions. This is because an applied high ultrasonic frequency could provide great energy input in the melt pool, which effectively reduces the nucleation barrier [44,45], increases the nucleation rate, and ultimately refines the γ matrix grains. Moreover, the intense cavitation effect at 20 kHz might produce transient high-pressure pulses and micro-jets, which could disrupt the solidification front of alloys, thus greatly facilitating the columnar-to-equiaxed transition of the matrix grains [50]. Additionally, the enhancement of melt-pool convection at the high frequency of 20 kHz could promote the solute homogenization and uniform nucleation, which can weaken the crystallographic texture of deposited Inconel 718 alloys [51]. Also, the observed homogeneous KAM distribution in the 20-UA-DED sample was consistent with fine, nearly equiaxial γ grains with random orientation.

3.6. X-Ray Residual Stress Analysis

Figure 15 displays the residual macroscopic stresses measured in thin-walled Inconel 718 samples deposited under ultrasonic frequency modulation. It can be seen that the stresses in both the X and Z directions were compressive, with the magnitude in the X

direction approximately being three times greater than that in the Z direction. Moreover, as the ultrasonic frequency was increased from 12 kHz to 16 kHz and then to 20 kHz, the compressive stresses in the two directions of the UA-DED samples gradually decreased, and the 20 kHz frequency deposited sample was almost in a stress-free state (–35 MPa) along the Z direction.

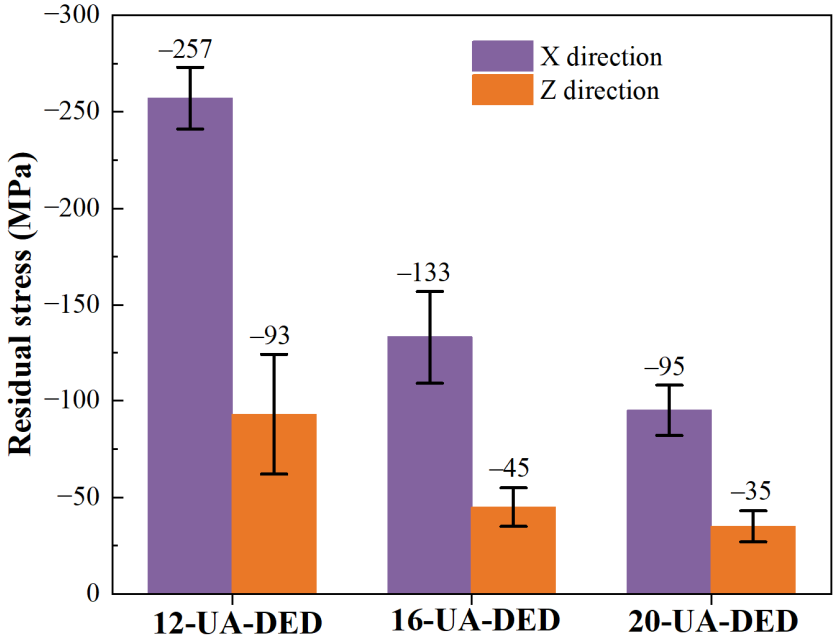


Figure 15. Residual stress of the UA-DED thin-walled Inconel 718 samples.

The frequency-dependent variations in the residual macroscopic stress observed in the UA-DED Inconel 718 samples might be associated with the ultrasonic vibration-induced strain-hardening, composition/microstructure homogenization or softening effects [52,53]. Intuitively, the low-frequency ultrasonic vibration could induce cyclic strains within the melt pool during deposition, promoting the mobility and pile-up of GNDs [54] and thereby contributing to strain hardening of the alloys to some extent. This strain-hardening effect most likely led to large stresses in the as-deposited alloys. In contrast, the high-frequency ultrasonic vibration can generate vigorous agitation within the melt pool. This action significantly homogenized both the elemental composition (Section 3.4) and the microstructures (Sections 3.3 and 3.5) and possibly enhanced the subsequent dynamic recovery of the alloys. The resulting uniformity in composition and microstructure, combined with this potential softening effect, effectively alleviated the thermal stresses induced during deposition. Consequently, the high-frequency UA-DED sample exhibited low macroscopic residual stresses.

3.7. Tensile Properties

The room-temperature tensile properties of the thin-walled Inconel 718 samples deposited via ultrasonic frequency modulation were evaluated, and the representative stress–strain curves together with the relevant YS, UTS, and elongation data along the Z and X directions are presented in Figure 16. It can be observed that as the ultrasonic frequency was modulated from 12 kHz to 16 kHz and then to 20 kHz, the YS were nearly unchanged for the samples loaded along either the Z or the X direction, while for the UTS of samples, it increased from 807 MPa to 861 MPa and then to 877 MPa along the X direction and remained constant along the other direction. Most importantly, the application of a high ultrasonic frequency led to a significant improvement in the elongation of the as-deposited

samples in both directions. Specifically, the elongation increased by a total of 41% along the Z direction and by 58% along the X direction. Consequently, the 20-UA-DED sample exhibited superior mechanical properties, with a YS of 465 MPa (416 MPa), a UTS of 899 MPa (877 MPa), and an elongation of 34.8% (38.9%) when loaded along the Z (X) direction.

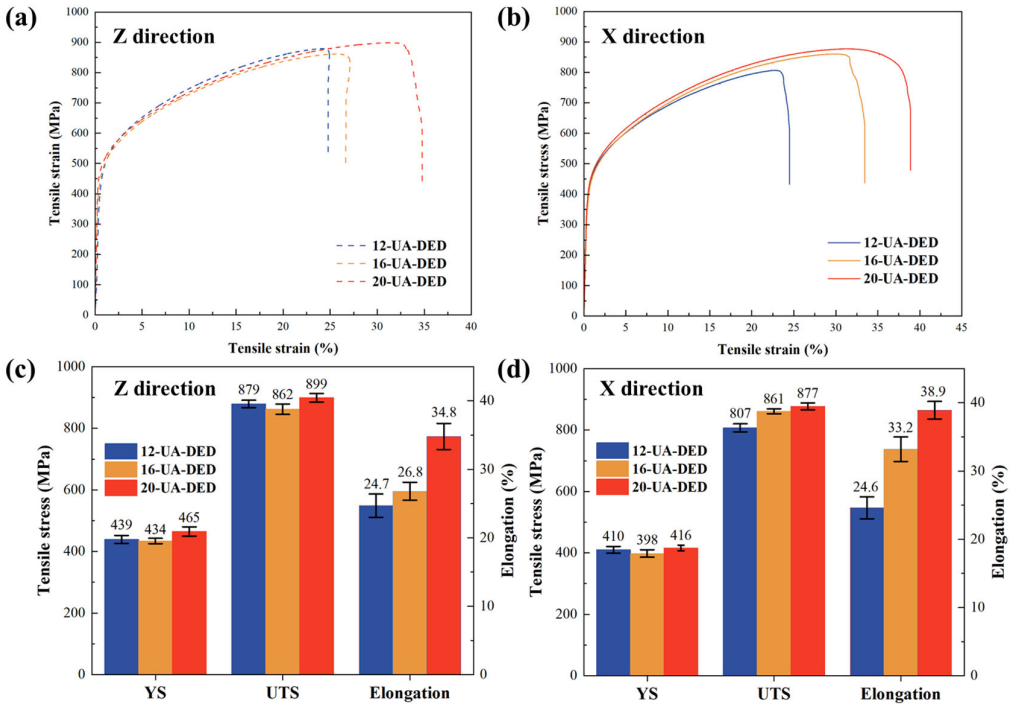


Figure 16. Tensile properties of thin-walled Inconel 718 samples deposited under ultrasonic frequency modulation: stress–strain curves along (**a**) the Z direction and (**b**) the X direction as well as the relevant strength and elongation data along (**c**) the Z direction and (**d**) the X direction.

The negligible variation of YS for these UA-DED samples was probably due to their similar microstructure characteristics, including the substructure (i.e., the domain size and microstrain as specified in Section 3.2), basically coarse matrix grains with sizes exceeding 20 μm (Section 3.5), and KAM values (i.e., the GND density as specified in Section 3.5), which were thought to provide the same resistance to the onset of dislocation glide [55]. Moreover, the enhancement of UTS with increasing ultrasonic frequency along the X direction might originate from the decrease of porosity (Figure 5), reduction of the fragmented Laves phase (Figure 8), the mitigation of Nb/Mo segregation (Figure 10 and Table 3), an increase in the grain boundary density (grain refinement in Figure 11), and the homogeneous distribution of KAM (Figure 14), which collectively enhanced the work-hardening capacity of the samples during plastic deformation [51]. Such increased work-hardening capacity could effectively delay the onset of necking instability [56], thereby enhancing the UTS. Furthermore, when the samples loaded along the Z (build) direction, the UTS might be governed by the bonding quality between interlayers [57], which was possibly independent of the magnitude of ultrasonic frequencies applied during deposition.

The significant improvement in ductility of the UA-DED samples can be attributed to several interrelated microstructural effects induced by high-frequency ultrasonic vibration. First, the refined and uniform microstructure with homogeneous elemental composition in the high-frequency UA-DED sample helped alleviate stress concentration, delay damage initiation, and hinder microcrack propagation during tensile loading [58]. Second, the increased density of grain boundaries produced at high ultrasonic frequencies acted as effective barriers to crack propagation [59]. Additionally, the random crystallographic orien-

tation in the high-frequency UA-DED sample promoted homogeneous plastic deformation by enabling a great number of grains to favorably align their dislocation slip systems under macroscopic stress [60]. Furthermore, the homogeneous distribution of GNDs—particularly evident in the 20-UA-DED sample—facilitated strain accommodation across grain boundaries [61] and helped stabilize localized strain regions during tension [62]. Consequently, increasing the ultrasonic frequency substantially enhanced the ductility of the as-deposited samples under loading along both the Z and X directions.

Figure 17 presents the tensile fracture morphologies (Z direction) of the UA-DED thin-walled Inconel 718 samples. Both the 12 kHz and 20 kHz deposited samples displayed typical ductile fracture features, characterized by the presence of high-density dimples resulting from microvoid nucleation, growth, and coalescence [63]. A comparison between Figure 17a,b revealed that the dimples in the 20 kHz UA-DED sample were notably finer and more densely distributed than those in its 12 kHz counterpart, suggesting improved mechanical properties for the former.

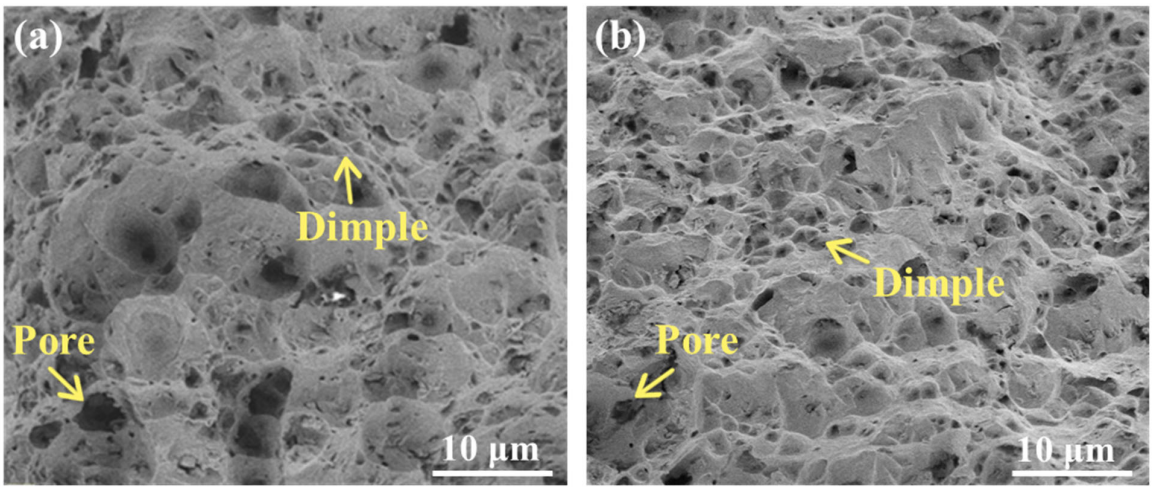


Figure 17. Representative fracture morphologies of the thin-walled Inconel 718 tensile test samples: (**a**) 12-UA-DED and (**b**) 20-UA-DED.

4. Conclusions

In summary, this study demonstrated that 20 kHz is the optimal ultrasonic frequency for tailoring the microstructure and mechanical properties of UA-DED thin-walled Inconel 718 alloys. At this frequency, the enhanced cavitation and acoustic streaming can eliminate large pores and reduce porosity to 0.08%. Meanwhile, the microstructure is refined and homogenized, featuring fine and nearly equiaxed γ grains, a fragmented and reduced Laves phase, uniformly distributed nanoscale γ'/γ'' precipitates, and a three-dimensionally uniform arrangement of GNDs. These microstructural improvements collectively enhance the UTS, increase the ductility by up to 58%, and reduce the residual stresses through the composition-microstructure homogenization and potential dynamic recovery. This work provides important insights into the microstructural control and mechanical property optimization in the ultrasonic-assisted additive manufacturing of nickel-based superalloys. Future studies will focus on evaluating long-term high-temperature performance under extreme service conditions, thereby facilitating the engineering application of this process for fabricating complex thin-walled Inconel 718 components in the aerospace field.

Author Contributions: Conceptualization, B.P., X.Z. and F.B.; methodology, B.P., M.Z. and Z.C.; investigation, B.P. and Z.C.; formal analysis, X.Z., M.Z. and F.B.; writing—original draft preparation, B.P.; writing—review and editing, B.P., Z.C. and X.C.; supervision, Z.C. and X.C. All authors have read and agreed to the published version of the manuscript.

Funding: This research received no external funding.

Data Availability Statement: The original contributions presented in this study are included in the article. Further inquiries can be directed to the corresponding authors.

Conflicts of Interest: Author Fahai Ba was employed by the company Shanghai Research Institute of Materials Co., Ltd. The remaining authors declare that the research was conducted in the absence of any commercial or financial relationships that could be construed as a potential conflict of interest.

References

1. Hosseini, E.; Popovich, V.A. A review of mechanical properties of additively manufactured Inconel 718. *Addit. Manuf.* **2019**, *30*, 100877. [CrossRef]
2. Panigrahi, S.K.; Sarangi, N.; Chandrasekhar, U. Experimental evaluation of overload capability of an annular combustor casing of a gas turbine engine. *Exp. Tech.* **2016**, *40*, 841–848. [CrossRef]
3. Prasad, K.S.; Panda, S.K.; Kar, S.K.; Sen, M.; Murty, S.V.S.N.; Sharma, S.C. Microstructures, forming limit and failure analyses of Inconel 718 sheets for fabrication of aerospace components. *J. Mater. Eng. Perform.* **2017**, *26*, 1513–1530. [CrossRef]
4. Deffley, R.J. Development of Processing Strategies for the Additive Layer Manufacture of Aerospace Components in Inconel 718. Ph.D. Thesis, University of Sheffield, Sheffield, UK, 2012.
5. Kumar, S.P.; Elangovan, S.; Mohanraj, R.; Ramakrishna, J.R. A review on properties of Inconel 625 and Inconel 718 fabricated using direct energy deposition. *Mater. Today Proc.* **2021**, *46*, 7892–7906. [CrossRef]
6. Alqawasmi, L.; Bijjala, S.T.; Khraishi, T.; Kumar, P. Mechanical property heterogeneity in Inconel 718 superalloy manufactured by directed energy deposition. *J. Mater. Sci.* **2024**, *59*, 5047–5065. [CrossRef]
7. Godec, M.; Malej, S.; Feizpour, D.; Donik, Č.; Balažic, M.; Klobčar, D.; Pambaguian, L.; Conradi, M.; Kocijan, A. Hybrid additive manufacturing of Inconel 718 for future space applications. *Mater. Charact.* **2021**, *172*, 110842. [CrossRef]
8. Cavalcante, T.R.F.; Mariani, F.E.; Diaz, J.A.A. Additive manufacturing of Inconel 718: A review on microstructures and mechanical properties of DED-LB-processed samples. *J. Mater. Res.* **2025**, 1–23. [CrossRef]
9. Chen, Y.; Zhou, Q. Directed energy deposition additive manufacturing of CoCrFeMnNi high-entropy alloy towards densification, grain structure control and improved tensile properties. *Mater. Sci. Eng. A* **2022**, *860*, 144272. [CrossRef]
10. Ma, D.; Stoica, A.D.; Wang, Z.; Beese, A.M. Crystallographic texture in an additively manufactured nickel-base superalloy. *Mater. Sci. Eng. A* **2017**, *684*, 47–53. [CrossRef]
11. Liu, W.; Zou, B.; Wang, X.; Ding, S.; Liu, J.; Li, L.; Huang, C.; Yao, P. Tailored microstructure and enhanced high temperature behavior of TiC/Inconel 718 composites through dual-gradient printing strategy in direct energy deposition. *J. Mater. Process. Technol.* **2025**, *336*, 118679. [CrossRef]
12. Aydinöz, M.E.; Brenne, F.; Schaper, M.; Schaak, C.; Tillmann, W.; Nellesen, J.; Niendorf, T. On the microstructural and mechanical properties of post-treated additively manufactured Inconel 718 superalloy under quasi-static and cyclic loading. *Mater. Sci. Eng. A* **2016**, *669*, 246–258. [CrossRef]
13. Wu, Z.; Narra, S.P.; Rollett, A. Exploring the fabrication limits of thin-wall structures in a laser powder bed fusion process. *Int. J. Adv. Manuf. Technol.* **2020**, *110*, 191–207. [CrossRef]
14. Han, S.B.; Lee, Y.; Lee, H.; Jang, J.S.; Park, S.H.; Song, H. Tailoring solidification and strength enhancement through process parameter optimization in Nb-added 316L stainless steel fabricated by directed energy deposition (DED). *J. Mater. Res. Technol.* **2025**, *39*, 4532–4543. [CrossRef]
15. Chen, Y.; Guo, Y.; Xu, M.; Ma, C.; Zhang, Q.; Wang, L.; Yao, J.; Li, Z. Study on the element segregation and Laves phase formation in the laser metal deposited IN718 superalloy by flat top laser and gaussian distribution laser. *Mater. Sci. Eng. A* **2019**, *754*, 339–347. [CrossRef]
16. Schirra, J.J.; Caless, R.H.; Hatala, R.W. The effect of Laves phase on the mechanical properties. In *Superalloys 718, 625 and Various Derivatives*; The Minerals, Metals & Materials Society (TMS): Pittsburgh, PA, USA, 1991; pp. 375–388.
17. Li, C.; Liu, Z.Y.; Fang, X.Y.; Guo, Y.B. Residual stress in metal additive manufacturing. *Procedia CIRP* **2018**, *71*, 348–353. [CrossRef]
18. Wang, F.; Del Bosque, H.; Hyder, J.; Corliss, M.; Hung, W.N. Experimental investigation of porosity distribution in selective laser melted Inconel 718. *Procedia Manuf.* **2020**, *48*, 807–813. [CrossRef]
19. Yang, Z.; Wang, S.; Zhu, L.; Ning, J.; Xin, B.; Dun, Y.; Yan, W. Manipulating molten pool dynamics during metal 3D printing by ultrasound. *Appl. Phys. Rev.* **2022**, *9*, 021416. [CrossRef]
20. Zhang, W.; Xu, C.; Li, C.; Wu, S. Advances in ultrasonic-assisted directed energy deposition (DED) for metal additive manufacturing. *Crystals* **2024**, *14*, 114. [CrossRef]
21. Yang, Z.; Zhu, L.; Dun, Y.; Ning, J.; Wang, S.; Xue, P.; Xu, P.; Yu, M.; Yan, B.; Xin, B. In-situ monitoring of the melt pool dynamics in ultrasound-assisted metal 3D printing using machine learning. *Virtual Phys. Prototyp.* **2023**, *18*, e2251453. [CrossRef]

22. Fang, Y.; Yamamoto, T.; Komarov, S. Cavitation and acoustic streaming generated by different sonotrode tips. *Ultrason. Sonochem.* **2018**, *48*, 79–87. [CrossRef]
23. Wang, S.; Kang, J.; Guo, Z.; Lee, T.L.; Zhang, X.; Wang, Q.; Deng, C.; Mi, J. In situ high speed imaging study and modelling of the fatigue fragmentation of dendritic structures in ultrasonic fields. *Acta Mater.* **2019**, *165*, 388–397. [CrossRef]
24. Han, J.; Wang, S.; Ge, W.; Chen, H.; Sun, Y.; Ai, Y.; Yuan, W.; Ruan, S.; Niu, W.; Yang, H.; et al. Non-contact ultrasound to assist laser additive manufacturing. *Nat. Commun.* **2025**, *16*, 7613. [CrossRef] [PubMed]
25. Zhang, T.; Li, P.; Zhou, J.; Wang, C.; Meng, X.; Huang, S. Microstructure evolution of laser cladding Inconel 718 assisted hybrid ultrasonic-electromagnetic field. *Mater. Lett.* **2021**, *289*, 129401. [CrossRef]
26. Han, J.; Chen, H.; Huang, Y.; Xiang, L.; Tao, J.; Lin, X. Printability and grain refinement in stainless steel processed by non-contact ultrasound-assisted additive manufacturing. *J. Mater. Res. Technol.* **2025**, *39*, 548–557. [CrossRef]
27. Ning, F.; Hu, Y.; Liu, Z.; Wang, X.; Li, Y.; Cong, W. Ultrasonic vibration-assisted laser engineered net shaping of Inconel 718 parts: Microstructural and mechanical characterization. *J. Manuf. Sci. Eng.* **2018**, *140*, 061012. [CrossRef]
28. Yang, Z.; Zhu, L.; Ning, J.; Wang, S.; Xue, P.; Xu, P.; Dun, Y.; Xin, B.; Zhang, G. Revealing the Influence of Ultrasound/Heat Treatment on Microstructure Evolution and Tensile Failure Behavior in 3D-Printing of Inconel 718. *J. Mater. Process. Technol.* **2022**, *305*, 117574. [CrossRef]
29. Zhou, H.; Yang, Y.; Han, C.; Liu, L.; Yan, Z.; Wei, Y.; Jiang, R.; Chen, X.; Wang, D. Microstructure and mechanical properties of GH4169 thin-walled parts fabricated by ultrasonic vibration assisted laser directed energy deposition/milling hybrid process. *Thin-Walled Struct.* **2024**, *205*, 112349. [CrossRef]
30. Peng, B.; Zhang, X.; Zhang, M.; Chai, Z.; Ba, F.; Chen, X. Microstructure and mechanical property of thin-walled Inconel 718 parts fabricated by ultrasonic-assisted laser-directed energy deposition. *Crystals* **2025**, *15*, 815. [CrossRef]
31. Yang, Z.; Zhu, L.; Wang, S.; Ning, J.; Dun, Y.; Meng, G.; Xue, P.; Xu, P.; Xin, B. Effects of ultrasound on multilayer forming mechanism of Inconel 718 in directed energy deposition. *Addit. Manuf.* **2021**, *48*, 102462. [CrossRef]
32. Wang, Y.; Shi, B.; Xu, C.; Li, X.; Yu, Y.; Zhu, Z.; Xu, R. Ultrasonic-assisted laser directed energy deposition of Inconel 718 alloy. *SSRN Prepr.* **2025**. [CrossRef]
33. Wang, H.; Hu, Y.; Ning, F.; Cong, W. Ultrasonic vibration-assisted laser engineered net shaping of Inconel 718 parts: Effects of ultrasonic frequency on microstructural and mechanical properties. *J. Mater. Process. Technol.* **2020**, *276*, 116395. [CrossRef]
34. Ning, F.; Jiang, D.; Liu, Z.; Wang, H.; Cong, W. Ultrasonic frequency effects on the melt pool formation, porosity, and thermal-dependent property of Inconel 718 fabricated by ultrasonic vibration-assisted directed energy deposition. *J. Manuf. Sci. Eng.* **2021**, *143*, 051009. [CrossRef]
35. Postema, M.; Marmottant, P.; Lancée, C.T.; Hilgenfeldt, S.; de Jong, N. Ultrasound-induced microbubble coalescence. *Ultrasound Med. Biol.* **2004**, *30*, 1337–1344. [CrossRef] [PubMed]
36. Ye, L.; Zhu, X.; He, Y. Micro-cutting force model of micro-jet induced by cavitation collapse in the ultrasonic field at micro-nano scale. *Int. J. Adv. Manuf. Technol.* **2022**, *119*, 3695–3702. [CrossRef]
37. Van Reet, J.; Tunnell, K.; Anderson, K.; Kim, H.-C.; Kim, E.; Kowsari, K.; Yoo, S.-S. Evaluation of advective solute infiltration into porous media by pulsed focused ultrasound-induced acoustic streaming effects. *Ultrasonography* **2023**, *43*, 35–46. [CrossRef]
38. Zhao, Z.; Li, L.; Yang, W.; Zeng, Y.; Lian, Y.; Yue, Z. A comprehensive study of the anisotropic tensile properties of laser additive manufactured Ni-based superalloy after heat treatment. *Int. J. Plast.* **2022**, *148*, 103147. [CrossRef]
39. Sumiya, H.; Toda, N.; Nishibayashi, Y.; Satoh, S. Crystalline perfection of high purity synthetic diamond crystal. *J. Cryst. Growth* **1997**, *178*, 485–494. [CrossRef]
40. Chai, Z.; Huang, X.; Xu, J.; Yu, Z.; Ji, V.; Jiang, C.; Chen, X. Kinetics and energetics of room-temperature microstructure in nanocrystalline Cu films: The grain-size dependent intragrain strain energy. *J. Appl. Phys.* **2022**, *131*, 5. [CrossRef]
41. David, W.I.F.; Leoni, M.; Scardi, P. Domain size analysis in the Rietveld method. *Mater. Sci. Forum* **2010**, *651*, 187–200. [CrossRef]
42. Abdel-Rahman, A.S.; Sabry, Y.A. An approach to the micro-strain distribution inside nanoparticle structure. *Int. J. Non-Linear Mech.* **2024**, *161*, 104670. [CrossRef]
43. Li, P.; Wang, Z.; Diao, M.; Guo, C.; Wang, J.; Zhao, C.; Jiang, F. Dynamic recrystallization and recovery in very high-power ultrasonic additive manufacturing. *Adv. Eng. Mater.* **2021**, *23*, 2000958. [CrossRef]
44. Alexander, A.J.; Camp, P.J. Single pulse, single crystal laser-induced nucleation of potassium chloride. *Cryst. Growth Des.* **2009**, *9*, 958–963. [CrossRef]
45. Lee, J.; Yang, S. Antisolvent sonocrystallisation of sodium chloride and the evaluation of the ultrasound energy using modified classical nucleation theory. *Crystals* **2018**, *8*, 320. [CrossRef]
46. Manikandan, S.G.K.; Sivakumar, D.; Rao, K.P.; Kamaraj, M. Effect of weld cooling rate on Laves phase formation in Inconel 718 fusion zone. *J. Mater. Process. Technol.* **2014**, *214*, 358–364. [CrossRef]
47. Cieslak, M.J.; Knorovsky, G.A.; Headley, T.J.; Romig, A.D., Jr. *The Solidification Metallurgy of Alloy 718 and Other Nb-Containing Superalloys*; Technical Report; Sandia National Laboratories: Albuquerque, NM, USA, 1988.

48. Xiao, H.; Li, S.; Han, X.; Mazumder, J.; Song, L. Laves phase control of Inconel 718 alloy using quasi-continuous-wave laser additive manufacturing. *Mater. Des.* **2017**, *122*, 330–339. [CrossRef]
49. Li, X.; Fang, X.; Zhang, M.; Wang, B.; Huang, K. Enhanced strength–ductility synergy of magnesium alloy fabricated by ultrasound assisted directed energy deposition. *J. Mater. Sci. Technol.* **2024**, *178*, 247–261. [CrossRef]
50. Guo, J.; Wang, J.; Cheng, L.; Duan, Y.; Zhan, X. Unravelling the mechanism of columnar-to-equiaxed transition and grain refinement in ultrasonic vibration assisted laser welding of Ti6Al4V titanium alloy. *Ultrasonics* **2024**, *141*, 107342. [CrossRef]
51. Absar, S.; Pasumarthi, P.; Choi, H. Numerical and experimental studies about the effect of acoustic streaming on ultrasonic processing of metal matrix nanocomposites (MMNCs). *J. Manuf. Process.* **2017**, *28*, 515–522. [CrossRef]
52. Yuan, K.; Sumi, Y. Simulation of residual stress and fatigue strength of welded joints under the effects of ultrasonic impact treatment (UIT). *Int. J. Fatigue* **2016**, *92*, 321–332. [CrossRef]
53. Zhang, Q.; Yu, L.; Shang, X.; Zhao, S. Residual stress relief of welded aluminum alloy plate using ultrasonic vibration. *Ultrasonics* **2020**, *107*, 106164. [CrossRef]
54. Giang, N.A.; Seupel, A.; Kuna, M.; Hütter, G. Dislocation pile-up and cleavage: Effects of strain gradient plasticity on micro-crack initiation in ferritic steel. *Int. J. Fract.* **2018**, *214*, 1–15. [CrossRef]
55. Johnston, W.G.; Gilman, J.J. Dislocation velocities, dislocation densities, and plastic flow in lithium fluoride crystals. *J. Appl. Phys.* **1959**, *30*, 129–144. [CrossRef]
56. Ghosh, A.K. Tensile instability and necking in materials with strain hardening and strain-rate hardening. *Acta Metall.* **1977**, *25*, 1413–1424. [CrossRef]
57. Foster, B.K.; Beese, A.M.; Keist, J.S.; McHale, E.T.; Palmer, T.A. Impact of interlayer dwell time on microstructure and mechanical properties of nickel and titanium alloys. *Metall. Mater. Trans. A* **2017**, *48*, 4411–4422. [CrossRef]
58. Hasani, N.; Dharmendra, C.; Sanjari, M.; Fazeli, F.; Amirkhiz, B.S.; Pirgazi, H.; Janaki Ram, G.D.; Mohammadi, M. Laser powder bed fused Inconel 718 in stress-relieved and solution heat-treated conditions. *Mater. Charact.* **2021**, *181*, 111499. [CrossRef]
59. Chen, Y.Q.; Pan, S.P.; Zhou, M.Z.; Yi, D.Q.; Xu, D.Z.; Xu, Y.F. Effects of inclusions, grain boundaries and grain orientations on the fatigue crack initiation and propagation behavior of 2524-T3 Al alloy. *Mater. Sci. Eng. A* **2013**, *580*, 150–158. [CrossRef]
60. Barrett, C.D.; El Kadiri, H.; Tschopp, M.A. Breakdown of the Schmid law in homogeneous and heterogeneous nucleation events of slip and twinning in magnesium. *J. Mech. Phys. Solids* **2012**, *60*, 2084–2099. [CrossRef]
61. Jiang, J.; Britton, T.B.; Wilkinson, A.J. Evolution of intragranular stresses and dislocation densities during cyclic deformation of polycrystalline copper. *Acta Mater.* **2015**, *94*, 193–204. [CrossRef]
62. Yang, B.; Wei, B.; Fu, W.; Ye, P.; Wang, X.; Fang, W.; Li, X.; Li, R.; Wu, H.; Fan, G. Effect of interfacial reaction layers on crack propagation behavior of Ti/Al layered metal composites in uniaxial tensile test from the perspective of local strain. *Mater. Sci. Eng. A* **2025**, *942*, 148669. [CrossRef]
63. Bennani, B.; Picart, P.; Oudin, J. Some basic finite element analysis of microvoid nucleation, growth and coalescence. *Eng. Comput.* **1993**, *10*, 409–421. [CrossRef]

Disclaimer/Publisher's Note: The statements, opinions and data contained in all publications are solely those of the individual author(s) and contributor(s) and not of MDPI and/or the editor(s). MDPI and/or the editor(s) disclaim responsibility for any injury to people or property resulting from any ideas, methods, instructions or products referred to in the content.